Available online at www.sciencedirect.com
ScienceDirect
Acta Materialia 57 (2009) 5382–5395
Acta MATERIALIA
www.elsevier.com/locate/actamat

# Spatial correlation in grain misorientation distribution

Benoît Beausir [a,b,*], Claude Fressengeas [a], Nilesh P. Gurao [b], László S. Tóth [a], Satyam Suwas [b]

[a] Laboratoire de Physique et Mécanique des Matériaux, Université Paul Verlaine – Metz/CNRS, Ile du Saulcy, 57045 Metz, France
[b] Department of Materials Engineering, Indian Institute of Science, Bangalore 560012, India

Received 25 June 2009; received in revised form 20 July 2009; accepted 20 July 2009
Available online 21 August 2009

**Abstract**

Grain misorientation was studied in relation to the nearest neighbor's mutual distance using electron back-scattered diffraction measurements. The misorientation correlation function was defined as the probability density for the occurrence of a certain misorientation between pairs of grains separated by a certain distance. Scale-invariant spatial correlation between neighbor grains was manifested by a power law dependence of the preferred misorientation vs. inter-granular distance in various materials after diverse strain paths. The obtained negative scaling exponents were in the range of $-2 \pm 0.3$ for high-angle grain boundaries. The exponent decreased in the presence of low-angle grain boundaries or dynamic recrystallization, indicating faster decay of correlations. The correlations vanished in annealed materials. The results were interpreted in terms of lattice incompatibility and continuity conditions at the interface between neighboring grains. Grain-size effects on texture development, as well as the implications of such spatial correlations on texture modeling, were discussed.


*Keywords:* Misorientation; Spatial correlation; Geometrically necessary dislocations; Grain boundary; Internal stresses

## 1. Introduction

Studies of grain–boundary misorientation distributions commonly use the Mackenzie analysis [1]. In its original version, the analysis provides the probability density of misorientation between one grain and all other grains of a polycrystalline material while the modified version deals with correlated distribution. In this work only the misorientations between one grain and its nearest neighbors are shown. This representation is very useful in assessing the grain–boundary character as well as the influence of grain–boundary properties on mechanical behavior [2]. It has also been used to generate initial grain orientations for further simulations of texture development [3]. However, providing the distribution of misorientations and of grain–boundary types by their frequency of occurrence does not exhaust the description of the impact of grain boundaries on mechanical behavior. Texture development, recrystallization and many properties like fracture may also be controlled by the spatial arrangement of the grain–boundary orientation and misorientation distribution. For example, it has been suggested that *c*-axis orientation, polygonization and recrystallization in polycrystalline ice samples may be sensitive not only to grain-to-grain misorientation but also to spatial aspects such as grain size or boundary length between neighboring grains [4,5]. However, a general approach to the problem of defining a quantitative measure for the spatial non-uniformity of the grain–boundary distribution has not been developed so far. In particular, the Mackenzie distribution overlooks the potential dependence of grain–boundary misorientation on spatial aspects. It is therefore unable to reflect possible correlation between grain–boundary misorientation and any distance characterizing the pairs of neighboring grains. Yet, if such a spatial correlation exists, grains cannot be considered separately and independently. Moreover, their rotation rates must be connected, which will have a

* Corresponding author. Address: Laboratoire de Physique et Mécanique des Matériaux, Université Paul Verlaine – Metz/CNRS, Ile du Saulcy, 57045 Metz, France.
*E-mail address:* benoit.beausir@univ-metz.fr (B. Beausir).

1359-6454/$36.00 © 2009 Acta Materialia Inc. Published by Elsevier Ltd. All rights reserved.
doi:10.1016/j.actamat.2009.07.035

strong impact on the overall texture development. Indeed, Winther et al. [6] have shown that the variations in current grain orientations in a textured material are larger than those expected on the sole basis of differences in their initial orientations. These authors suggest that the unexpected variation is likely to originate in interactions with neighboring grains. Such spatial interactions are not properly accounted for in the polycrystal plasticity models currently used for the simulation of texture development, although in recent times there has been the opinion that this aspect should be taken into account. Spatial interactions are certainly not accounted for in approaches using the conventional Taylor or Sachs assumptions. Self-consistent models do consider interactions between a homogeneous grain and an equivalent infinite homogeneous matrix representing the rest of the material [7], but only in an average way, with no special consideration to length scales or to specific neighbor grains. Bolmaro et al. [8] and Tomé et al. [9] account for the interactions between neighbor grains in a two-sites self-consistent scheme, by enforcing the same lattice reorientation and maintaining the grains' relative misorientation, a condition dubbed "co-rotation" of neighbor grains. Crystal plasticity finite-element-based models dedicated to texture development simulation may account as well for interactions arising from the enforcement of continuity of the elastic spin at grain boundaries [10,11]. Finally the so-called LAMEL model [12–14] also accounts for interactions between a grain and its nearest neighbors by assuming continuity of some components of the traction and velocity gradient tensors at grain boundaries. All of these schemes tend to reduce the intensity of the simulated textures, in closer agreement with experimental results. However, the continuity conditions proposed in Refs. [8–14] clearly lack the understanding of the interactions between dislocation content of grain boundaries, internal stresses arising from grain–boundary incompatibility and deformation mechanisms in the neighboring grains.

Recent advances in the electron back-scattered diffraction technique (EBSD) give access to information such as the spatial location of grains in the scanned microstructure area. Therefore, an extension of the original Mackenzie analysis accounting, on a third axis, for some distance between grains now becomes feasible at reasonable expense and a quantitative measure for the spatial non-uniformity of the grain–boundary distribution is possible to establish. From this information, the objective of the present paper is to give evidence for, and characterize quantitatively, the grain-to-grain interactions. Further, it is to explain their origin as well as justify the need for "co-rotation type" schemes in texture modeling. In this aim, the probability for encountering a grain–boundary misorientation at a certain inter-granular distance has been systematically analyzed. Spatial correlations in grain–boundary misorientation distributions have been investigated in diverse microstructures spanning over a wide range of materials (pure and alloyed body-centered cubic (bcc), face-centered cubic (fcc) and hexagonal close packed (hcp) metals), under various loading conditions. In some deformation modes, process parameters like temperature and strain rate were also varied. In addition several heat treatments were performed after deformation in some samples. The rest of the paper is laid out as follows. In Section 2, the details of materials and experimental conditions are presented as well as a comprehensive account of the analysis. The actual experimental results are shown in Section 3. A discussion including an analysis of lattice incompatibility across grain boundaries follows in Section 4, with concluding remarks in Section 5.

## 2. Experiments

Table 1 includes the main features of the 21 experimental studies carried out to provide the background for this work, with details of the material, the nature of deformation and the respective experimental conditions. The tests used pure and alloyed metals, which were selected to be representative examples of the three main crystallographic structures, namely fcc, bcc and hcp. The fcc structure was sampled by nickel, copper, copper–0.3chromium and Cu–10Zn, the bcc structure by IF steel, and hcp by titanium, magnesium and Mg–3Al. The samples were deformed by torsion, tension, compression, symmetric or asymmetric rolling and equal channel angular extrusion (ECAE). In some experiments, two of these processes, such as ECAE and rolling, were used. As a consequence, the tests covered a wide range of plastic strain. Depending on the deformation mode, the equivalent von Mises (EQVM) strain achieved was in the range of 0.36–5.7. The tests were also conducted in different temperature and strain-rate conditions, from room temperature (RT) to 300 °C and from $10^{-4}$ $s^{-1}$ to 0.3 $s^{-1}$. After deformation, some of the samples were annealed for different periods of time to achieve different extent of static recrystallization. As a consequence of these treatments, the grain size of materials under investigation had a range from less than 1 μm in ECAEed materials to several tens of μm in other materials.

Table 1 is subdivided into four parts. Part 1 contains samples subjected to deformation only, whereas Part 2 includes samples that were deformed plus annealed. Several Mg samples in which dynamic recrystallization took place during the tests have been grouped in the third part. The last part of the table presents three samples of Cu–0.3Cr deformed by four ECAE passes, with two of them annealed at 500 °C for 5 and 60 min.

All samples were systematically examined through electron back-scattered diffraction (EBSD), using a FEI-SIRION field emission gun scanning electron microscope (FEG–SEM). Grain neighbors were identified and listed. From the measurements, each grain could be characterized by its orientation in the sample reference frame through its three Euler angles ($\varphi_1$, $\varphi$, $\varphi_2$) and, in complement, by its location in the scanned area. The elementary pixel was chosen to be a square-shaped pixel with a size ranging from 0.05 to 1 μm depending on the grain size. Sets of connected

Table 1
Experimental details.

| Part | No. | Material | Test | Temp. (°C) | EQVM | Strain-rate ($s^{-1}$) | Note | Nb. of grains | Nb. of pairs | Average diameter (μm) | Average distance (μm) |
|---|---|---|---|---|---|---|---|---|---|---|---|
| 1 | M1 | Cu | Torsion | RT | 5.70 | 0.3 | Recrystallization twins | 16,001 | 29,171 | 1.67 | 6.73 |
| | M2 | Cu | Torsion | RT | 4.66 | $10^{-2}$ | Recrystallization twins | 17,050 | 28,301 | 2.51 | 5.22 |
| | M3 | Cu | Torsion | RT | 4.10 | $10^{-4}$ | Mostly deformed grains | 16,575 | 27,164 | 0.63 | 0.98 |
| | M4 | Ti | Comp./X | RT | 0.36 | $3 \times 10^{-4}$ | Deformation twins | 2878 | 7039 | 6.82 | 15.3 |
| | M5 | Ti | Comp./Y | RT | 0.36 | $3 \times 10^{-4}$ | Deformation twins | 845 | 2162 | 5.83 | 10.9 |
| | M6 | Ni | Torsion | RT | 3.50 | $10^{-4}$ | Mostly deformed grains | 4206 | 9357 | 0.21 | 0.49 |
| | M7 | Cu–10Zn | Torsion | RT | 4.75 | 0.3 | Mostly deformed grains | 8638 | 20,903 | 1.02 | 1.30 |
| | M8 | Cu–10Zn | Torsion | RT | 2.00 | $10^{-4}$ | Mostly deformed grains | 28,371 | 71,235 | 0.54 | 0.86 |
| | M9 | Mg–3Al | Torsion | 250 | 0.45 | $10^{-4}$ | Mostly DRXed grains | 2213 | 5577 | 4.49 | 14.0 |
| | M10 | IF steel | ECAE 3Bc[a] | 300 | 3.46 | $\approx 2 \times 10^{-3}$ | Very small grains | 1685 | 1698 | 0.21 | 0.96 |
| 2 | M11 | Ni | Rolling | RT | 0.3 | $\approx 10^{-2}$ | Coarse grains, annealed 1200 °C 10 h | 185 | 423 | 146.2 | 231.6 |
| | M12 | Mg | ECAE 4Bc | 250 | 4.62 | $\approx 2.10^{-3}$ | Annealed 500 °C one hour | 1701 | 2589 | 23.9 | 109.3 |
| | M13 | Mg | ECAE 3Bc + rolling (80%) | 250 + RT | 4.59 | $\approx 2.10^{-3}$ | Annealed 500 °C one hour | 498 | 903 | 53.8 | 115.5 |
| 3 | M14 | Mg | ECAE 4A | 250 | 4.62 | $\approx 2 \times 10^{-3}$ | Mostly DRXed grains | 5224 | 9497 | 5.5 | 8.48 |
| | M15 | Mg | ECAE 4Bc | 250 | 4.62 | $\approx 2 \times 10^{-3}$ | Mostly DRXed grains | 6388 | 15,701 | 5.72 | 7.76 |
| | M16 | Mg | ECAE 4C | 250 | 4.62 | $\approx 2 \times 10^{-3}$ | Mostly DRXed grains | 4865 | 10,329 | 6.21 | 8.84 |
| | M17 | Mg | ECAE 3Bc + rolling (80%) | 250 + RT | 4.59 | $\approx 2 \times 10^{-3}$ | Mostly DRXed grains | 5328 | 7060 | 1.88 | 3.41 |
| | M18 | Mg | Asymmetric rolling | RT | ≈1.68 | $\approx 10^{-3}$ | Mostly DRXed grains | 7126 | 16,866 | 2.1 | 2.89 |
| 4 | M19 | Cu–0.3Cr | ECAE 4Bc | RT | 4.62 | $\approx 2 \times 10^{-3}$ | Mostly deformed grains | 11,065 | 23,797 | 0.36 | 0.74 |
| | M20 | Cu–0.3Cr | ECAE 4Bc | RT | 4.62 | $\approx 2 \times 10^{-3}$ | Annealed 500 °C 5 mn | 3789 | 9872 | 0.63 | 1.18 |
| | M21 | Cu–0.3Cr | ECAE 4Bc | RT | 4.62 | $\approx 2 \times 10^{-3}$ | Annealed 500 °C 60 mn | 5100 | 12,026 | 1.22 | 1.85 |

[a] "ECAE 3Bc" meaning 3 ECAE passes in route Bc.

and similarly oriented pixels (within a grain tolerance angle set to 5° for all samples) were grouped to define "grains". Thus, the minimum misorientation between two grains is 5°. Grains containing less than 2 pixels were not retained for the analysis. Although the pixel to pixel misorientation within a grain is small, the spread of orientation in a grain can be relatively large, as shown in Fig. 1. Once a grain is constructed in this manner, it is represented by the spatial position of its center of gravity in the 2D scan and an orientation that is the average of the orientation of all pixels constituting the grain. The scanned area was taken as large as possible in order to obtain satisfactory statistical sampling, with as many indexed grains and pairs of grains as possible (one pair is defined as a grain and one of its neighbors). The overall indexation rates were quite high and only the measurement points above 0.1 confidence index (CI) were considered (CI being a statistical measure of accuracy in automated indexing, with a scale of 0–1). Table 1 also includes the information about the number of indexed grains and the number of pairs of grains involved in each test. Using the Euler angles, and the orthogonal rotation tensor $\mathbf{R}$ mapping the sample reference frame onto the grain reference frame, the rotation between two neighbor grains $g_i$ and $g_j$ can be expressed by the tensor

$$\mathbf{M} = \mathbf{R}_{gi} \cdot \mathbf{R}^{\mathbf{t}}_{gj}, \tag{1}$$

where $\mathbf{R}_{gi}$ and $\mathbf{R}_{gj}$ are the rotation tensors of grains $g_i$ and $g_j$, respectively. The rotation angle $\theta_{ij}$ between grains $g_i$ and $g_j$ can be obtained from the tensor $\mathbf{M}$ as $\theta_{ij} = \arccos[(tr(\mathbf{M}) - 1)/2]$ [1]. Depending on the crystal structure, a number of symmetry matrices (24 for cubic and 12 for hexagonal metals) have to be applied on $\mathbf{R}_{gi}$ and $\mathbf{R}_{gj}$, to finally retain the minimum of $\theta_{ij}$ as the misorientation between the two grains [1]. In addition to misorientation, the distance $D_{ij} = |\mathbf{r}_i - \mathbf{r}_j|$ between the centers of gravity is calculated for each pair of grains. By complementing the conventional Mackenzie distribution with this distance information, we shall define the misorientation correlation function (MCF) as the probability density $f(\theta, D)$ for the joint occurrence of pairs of grains with misorientation $\theta$ and separated by distance $D$. Let us denote by $(\overline{\theta}, \overline{D})$ the intervals of length $(\Delta\theta, \Delta D)$ centered on the misorientation and distance values $(\theta, D)$, and $N(\overline{\theta}, \overline{D})$ the number of pairs of

grains simultaneously encountered in these two intervals. If $N$ is the total number of grains dealt with in the analysis, the probability density $f(\theta, D)$ is defined as

$$\frac{N(\bar{\theta},\overline{D})}{N} = \int_{\bar{\theta}} \int_{\overline{D}} f(\theta, D) d\theta dD. \quad (2)$$

It is normalized such that

$$\int_{\theta^*} \int_{D^*} f(\theta, D) d\theta dD = 1 \quad (3)$$

where $\theta^*$ and $D^*$ are the largest misorientation and distance intervals available in the EBSD map, respectively. In practice, $f(\theta, D)$ is approximated by the following summation:

$$f(\theta, D) \approx \frac{N(\bar{\theta},\overline{D})}{N\Delta\theta\Delta D} = \frac{1}{N\Delta\theta\Delta D} \sum_{i=1}^{N} \sum_{j=1}^{N} \chi_{\overline{D}}(D_i)\chi_{\bar{\theta}}(\theta_j). \quad (4)$$

Here use is made of the "indicator" functions $\chi_{\overline{D}}(D_i) = 1$, if $D_i \in \overline{D}$ and $\chi_{\overline{D}}(D_i) = 0$ otherwise, $\chi_{\bar{\theta}}(\theta_j) = 1$ if $\theta_j \in \bar{\theta}$ and $\chi_{\bar{\theta}}(\theta_j) = 0$ otherwise. Note that, as it is a probability density, $f(\theta, D)$ can be locally larger than one. Although it has differences with the orientation correlation function (OCF) introduced by Adams et al. [15], the MCF thus defined is very similar in spirit. We recall that the OCF is the probability density for the joint occurrence of grain orientation $g$ at a point P and orientation $g'$ at point P′, where (P, P′) are separated by a vector $\boldsymbol{r}$. Hence, the OCF describes a point-to-point crystal orientation correlation in real space, whereas the MCF is concerned with a grain-to-grain misorientation correlation accounting for grain-to-grain distance in an EBSD map. Also related to the MCF is the misorientation distribution function (MDF) defined by Bunge [16]. The MDF describes the probability that a grain boundary separates grains of a certain misorientation. However, any other information on distance than contiguity through grain boundary is overseen. Providing more detailed information than the MDF, while posing less formidable technical challenges than the OCF, the MCF adequately provides insights into microstructure analysis and possible spatial correlation in misorientation distribution. Thorough absence of spatial correlation should be reflected by a complete independence of the MCF on the grain-to-grain distance. The existence of a preferred distance and a preferred misorientation should translate into a Gaussian bell-shaped MCF. Spatial correlation arising from grain-to-grain interactions should give rise to monotonically decreasing MCFs with distance, as will be seen with more details in the next section. Note that, since all correlations are expected to vanish at large distances compared with the average grain size, only the nearest neighbors need to be considered in practice.

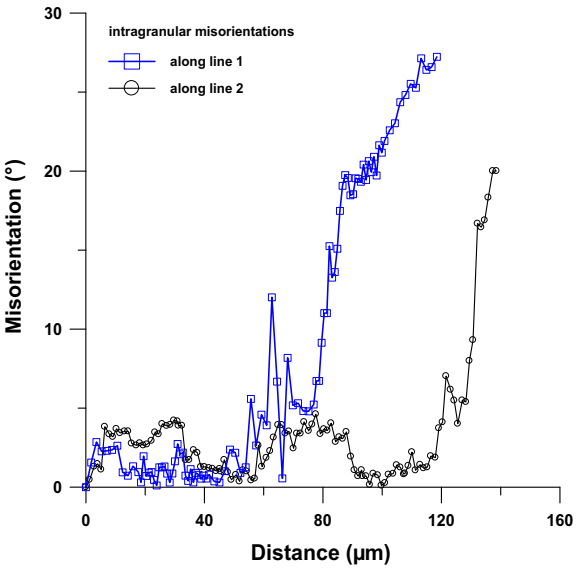


Fig. 1. Intra-granular misorientations in titanium compressed up to $\bar{\varepsilon} = 0.36$ (Material 4 in Table 1), see location of the lines in Fig. 3.

## 3. Results and analysis

Fig. 2 shows the MCF in four materials with distinct microstructural features such as twinning or dynamic recrystallization. Two limiting effects can be noted at once. At very short distances, a finite resolution effect is observed: the MCF drops down to zero, because there is a finite minimum grain size in the sample. Similarly, a finite size effect occurs at large distances: clearly, the MCF must also be zero when the inter-granular distance exceeds the size of the sample. Between these two extremes, the maps in Fig. 2a–c for Materials 1, 10 and 4, respectively (see Table 1) display marked maxima at short distances for specific misorientation angles, with monotonic decay of the MCF as the distance increases, which suggests that the preferred misorientations are mostly met at short inter-granular distances. Fig. 2a corresponds to a copper sample (Material 1 in Table 1) deformed in torsion up to $\bar{\varepsilon} = 5.7$ with an applied strain rate of 0.3 $s^{-1}$. Two distinct peaks are seen in the MCF. They correspond to primary and secondary recrystallization twins. The analysis shows that, under such conditions, primary recrystallization twins form in about 45% of the processed pairs of grains and secondary recrystallization twins in about 15–20%. The difference in the descending trend of the peaks suggests that primary recrystallization twins are twice as large as secondary twins, consistent with evidence that nucleation of secondary twins is constrained by primary twins. Fig. 2b shows an IF steel sample (Material 10 in Table 1, obtained by ECAE) with very small average grain size (about 0.2 μm). Primary recrystallization twins Σ3 and the CSL Σ13 are respectively present in about 15% and 25% of the pairs of grains investigated, and the MCF extends well beyond the average grain size. Fig. 2c shows titanium compressed up to $\bar{\varepsilon} = 0.36$ (Material 4 in Table 1). The figure shows that tensile and compressive twins with about the same size occur more frequently than low-angle grain boundaries and that they concern larger grains (see also the corresponding EBSD map in Fig. 3). In contrast, Fig. 2d shows a more even distribution with distance in Material 11 (annealed cold-rolled nickel), which suggests that the pre-

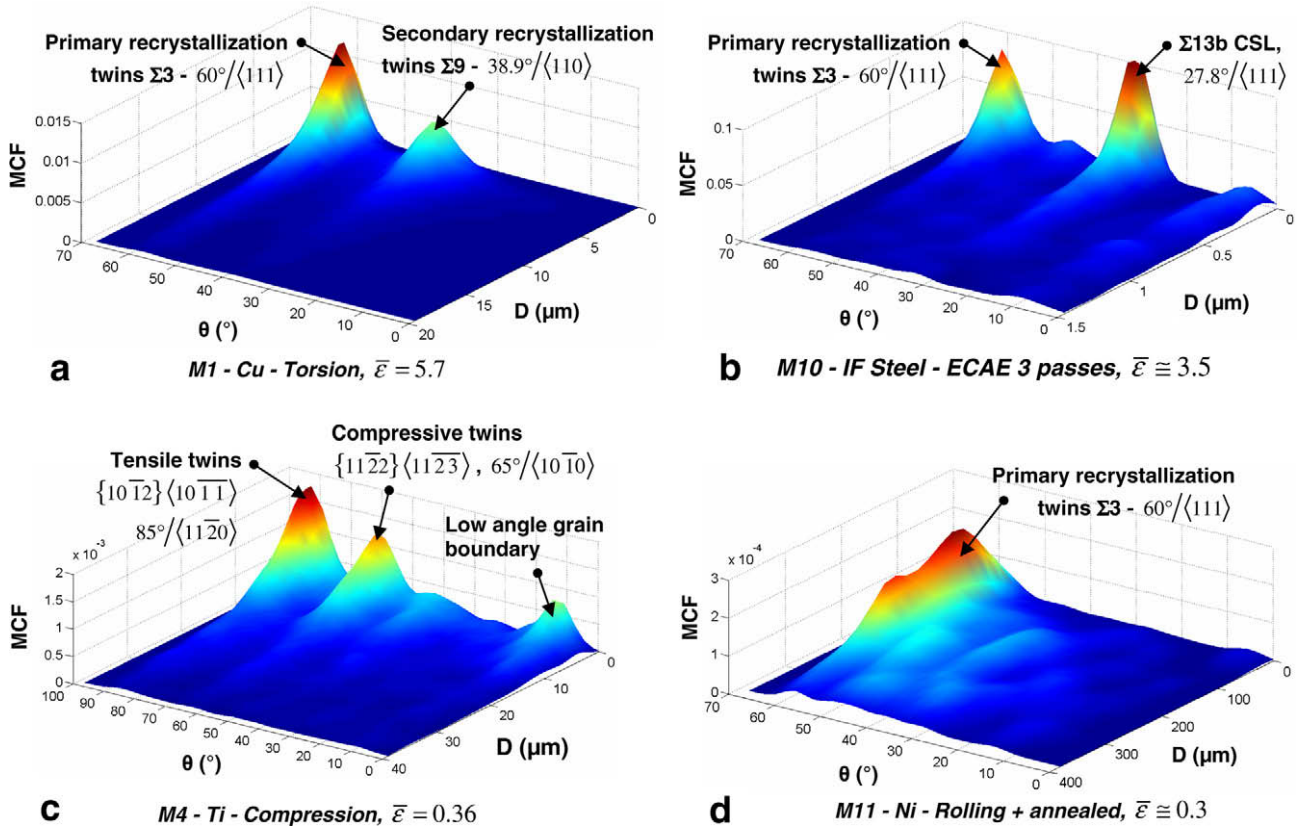


Fig. 2. Misorientation correlation function (MCF) of copper after torsion (a), IF steel after ECAE (b), titanium after compression (c) and rolled + annealed nickel (d).

ferred misorientation, corresponding to primary recrystallization twins Σ3, is met more uniformly in grains of all sizes.

The cross-sections of the three-dimensional distribution maps by constant misorientation planes were analyzed. In all cases considered in what follows but one explicitly mentioned, cross-sections are drawn through the maximum of the MCF, and the latter is provided as a function of the inter-granular distance $D$ in the selected plane. In all figures, the parts of the curves affected by the finite resolution effects at small and large distances are removed. Let us consider first the samples listed in Part 1 of Table 1 (including those in Fig. 2abc at preferred misorientations $\theta = 60°$, 30° and $\theta = 90°$, respectively), shown in logarithmic scale in Fig. 4a. In all the 10 cases, the curves can be fitted in power law form $F \propto d^{-\tau}$ with exponent $\tau = 2 \pm 0.3$. The finite size effect is clearly in evidence, as several curves bow in and depart from the linear trend at large distances. Remnants of the finite resolution effect can also be noticed, with the curve bowing in at short distances for some materials (Materials 1: copper in torsion, and 5: titanium in compression). It was checked that fitting the curves with exponential or Γ-function dependence was less convincing, as illustrated in Fig. 5 for the case of Material 1 (copper in torsion).

A power-law relationship $F \propto d^{-\tau}$ is indication of self-similarity of the dependency: regardless of the distance, the same scaling exponent $\tau$ describes the asymptotic behavior of $F$. Moreover, if the MCF satisfies the power law $F \propto d^{-\tau}$, it also obeys the functional equation $F(\lambda d) = \lambda^{-\tau} F(d)$ (and vice versa). This scaling symmetry implies that no characteristic length, i.e., no particular inter-granular distance is involved in the spatial dependence of the MCF. Thus, the power-law relationship suggests scale-invariant spatial correlation between neighboring grains. It is remarkable that this scaling behavior is found in materials with all major crystalline structures, irrespective of a particular loading path. It is valid for all the range of grain size in the material, from less than 1 μm in ECAEed IF steel (Material 10) to about 50 μm in titanium (Material 4). In order to ascertain the conjecture, surrogate sets of data were generated by disregistering grain misorientation and distance: specifically, misorientation and distance of a particular pair of grains were dissociated and randomly redistributed among the same set of grains. Clearly, the conventional Mackenzie distribution remains unaffected in the process, since it does not involve inter-granular distance. Similarly, crystallographic texture plots do not reveal any difference between the two data sets. The spatial dependency of the surrogate distributions is shown in Fig. 4b in logarithmic scales. It is clearly seen that the scale-invariant behavior is lost in the surrogate data. Instead, the misorientation first increases up to a preferred inter-granular distance, beyond which it decreases. A comparison with Fig. 4b confirms that the scaling behavior

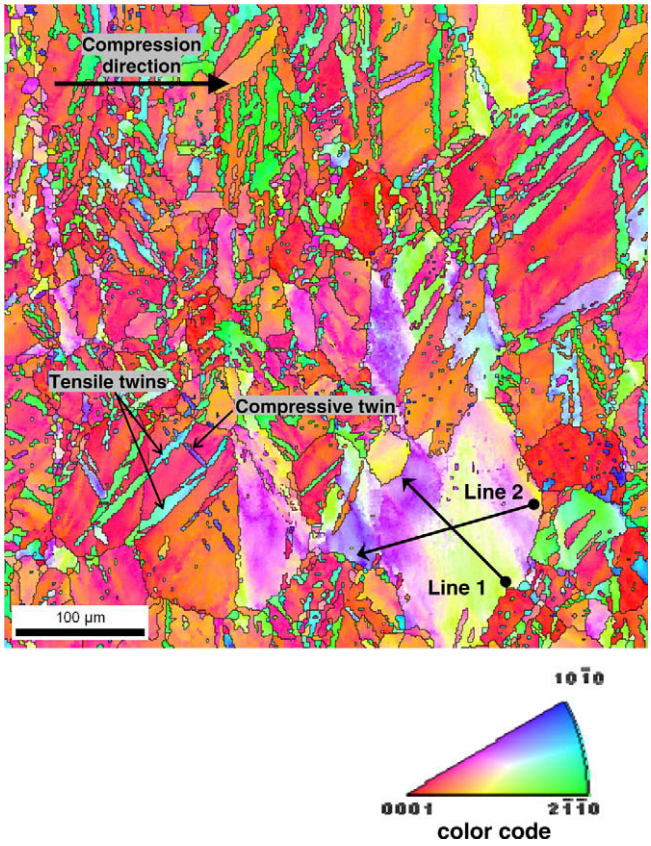


Fig. 3. Inverse pole figures of the transverse plane containing the compression direction in titanium compressed up to $\bar{\varepsilon} = 0.36$ (Material 4 in Table 1).

in Fig. 4a is linked with correct registry of the pairs of grains, and that on splitting misorientation and inter-granular distance, or ignoring distances, significant information is lost. Before considering Part 2 of Table 1, let us mention in addition that a cross-section of the distribution map for Material 4 through the local misorientation maximum ($\theta = 10°$) obtained for low-angle grain boundaries (see Fig. 2c) also displays scale-invariant spatial correlation, but with larger scaling exponent $\tau \cong 2.5$ suggesting faster decay (not shown in a figure) than for high-angle grain boundaries. When the misorientation angle is even smaller, spatial correlation is altogether absent, as seen from the flat distributions in Fig. 2.

In Part 2 of Table 1, materials listed were deformed and subsequently annealed (including Material 11 already shown in Fig. 2d). The cross-sections of the distribution maps by equal misorientation planes are shown in Fig. 6a. As could be guessed from Fig. 2d, fitting the curves with power laws cannot be worked out and, instead, preferred distances emerge from the analysis. Further, Fig. 6b shows that surrogate data sets built by randomly redistributing misorientations and distances among the pairs of grains as detailed above, does not result in any significant change in the curves. Hence, correct registry of the pairs of grains is indifferent in Fig. 6, and scale-invariant spatial correlations evidenced in the set of materials in Fig. 4a are clearly absent from the second set in Fig. 6. It is certainly tempting to attribute this absence of long distance correlation to the annealing treatment. Fig. 7a now presents the MCF vs. distance curves for the samples in Part 3 of Table 1. In those samples, significant dynamic recrystallization (DRX) was detected in the course of straining. The curves bow in at their upper left part, suggesting a quite even distribution at very short distances, but their decreasing lower right part can be fitted with a power law with exponent $\tau \cong 3.3$. Fig. 7b shows the corresponding curves for the surrogate data: the scaling behav-

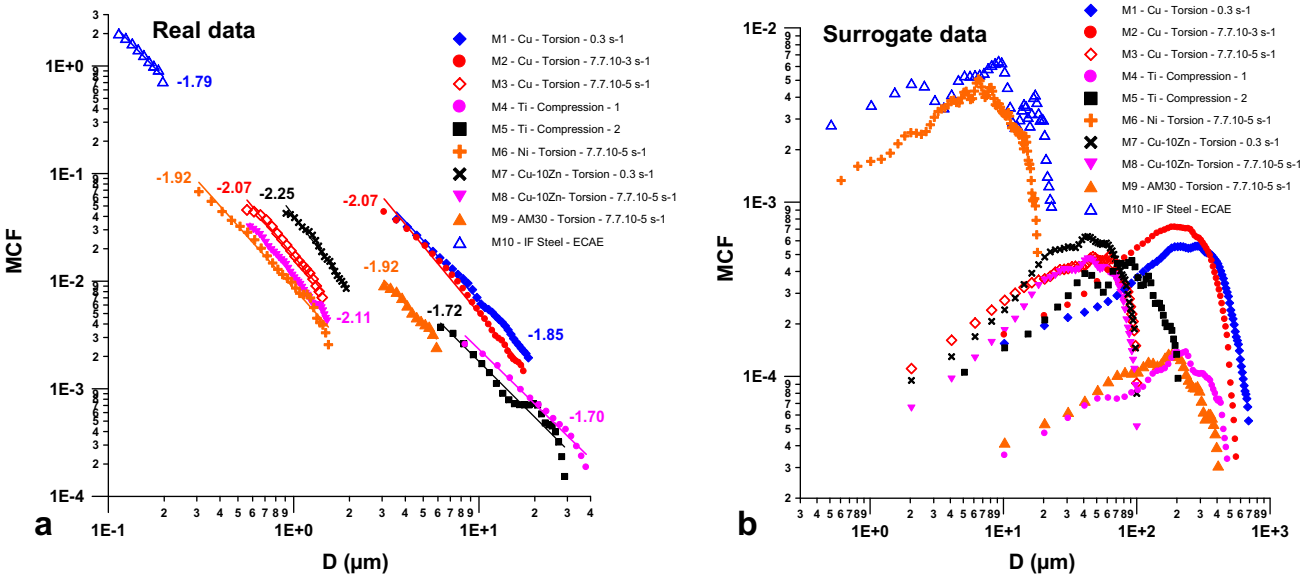


Fig. 4. Misorientation correlation functions (MCF) as function of distance $D$ for deformed samples (samples in Part 1 of Table 1) at preferred misorientation (a) as measured data and (b) surrogate data.

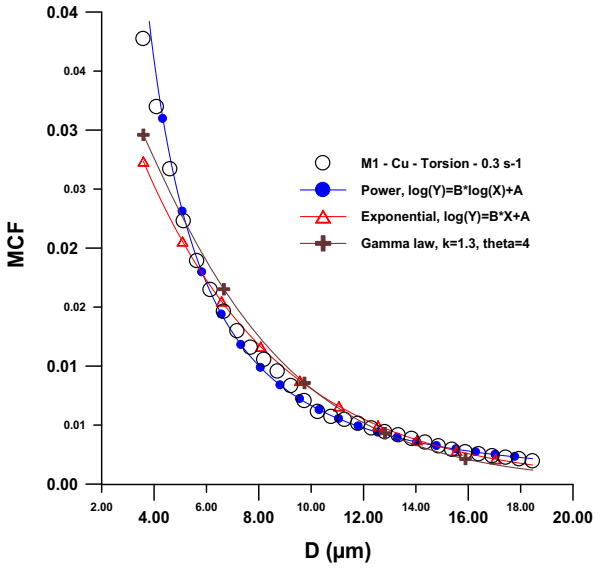


Fig. 5. Comparison of power law, exponential law and gamma law fittings on copper sample deformed in torsion at 0.3 $s^{-1}$ (Material 1).

ior present in Fig. 7a is clearly lost when randomization of distance vs. misorientation is plotted. Hence, the figure suggests scale-invariant spatial correlations, although with faster decay than in "only deformed" materials (Fig. 4a). Finally, the results for three Cu–0.3%Cr samples (Part 4 of Table 1) deformed up to four passes of ECAE, two of these samples being subsequently annealed at 500 °C for 5 and 60 min, respectively, are presented in Fig. 8 by iso-levels of the MCF. Real data are plotted in Fig. 8a–c, and surrogate data in Fig. 8d–f. Two preferred misorientations are seen at about 10° and 60° in purely deformed samples (Fig. 8a) with a maximum occurring at 0.3 μm. Note that the grain size obtained from the four ECAE passes amounts to 0.2 μm. After 5 min of annealing, the 10° misorientation maximum vanishes, while the 60° misorientation peak strongly increases and extends over the range (0.3–0.7 μm) (Fig. 8b). After annealing for 1 h, the grains grow by static recrystallization, which levels further the misorientation peak over the distance range (0.3–1.5 μm). Surrogate data (Fig. 8d–f) consistently show more homogeneous distribution than their real data counterparts. Cross-sections at 60° misorientation of these iso-level maps are plotted in Fig. 9a,b. As can be seen from Fig. 9a, scaling behavior with exponent $\tau \approx 2$ is obtained for the deformed sample in Fig. 8a, for the whole range of distances. When the material is annealed, the range of scaling behavior is degraded at short distances, where misorientation becomes more homogeneous and a preferred characteristic distance is seen. However, the slope $\tau \approx 2$ is still perceived on a shorter range at long distances. Clearly, these last two curves resemble more and more their surrogate data counterparts (see Fig. 9b). These results are clearly supporting the notion that annealing lessens spatial correlation in the misorientation distribution.

## 4. Discussion

### 4.1. Effect of measuring method

It might be argued, not unreasonably, that the results in Section 3 are relative to an EBSD map (a particular image of the material), but not to the material itself. For example, the analysis is such that a grain inside the map has no correlation with a grain outside the map, and, hence, there is map-dependency of the results. However, these effects impact primarily on grains located close to the borders of the map, and they are of limited concern once the number of grains processed in the map is made large enough (usually several thousands in our data sets). Similarly, maps are two-dimensional

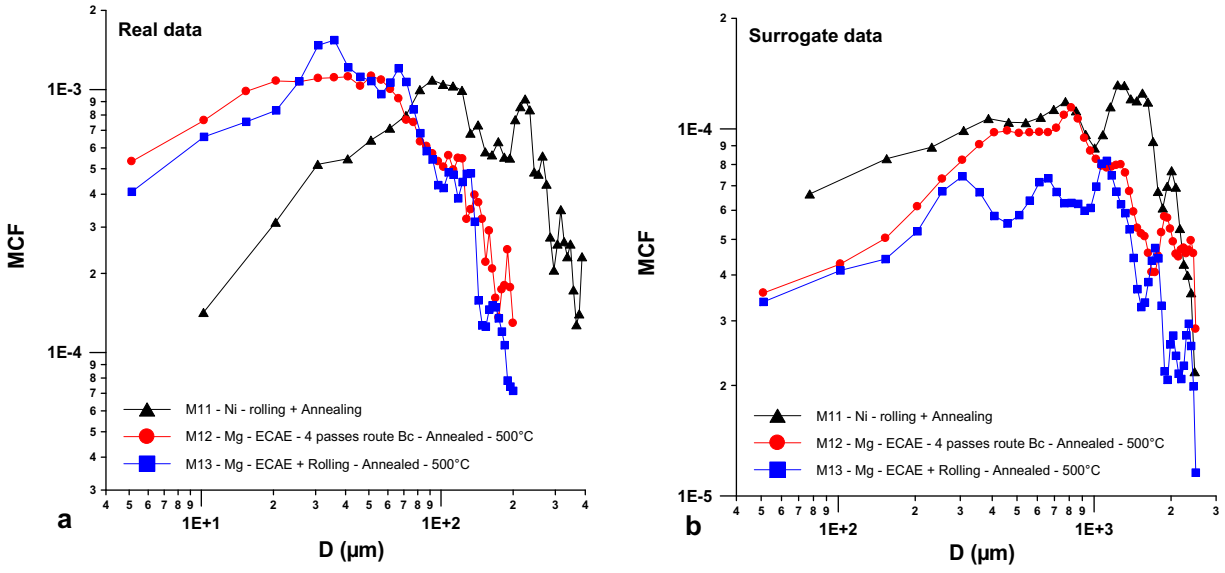


Fig. 6. Misorientation correlation functions (MCF) as function of distance $D$ for annealed samples (samples in Part 2 of Table 1) at preferred misorientation (a) as measured data and (b) surrogate data.

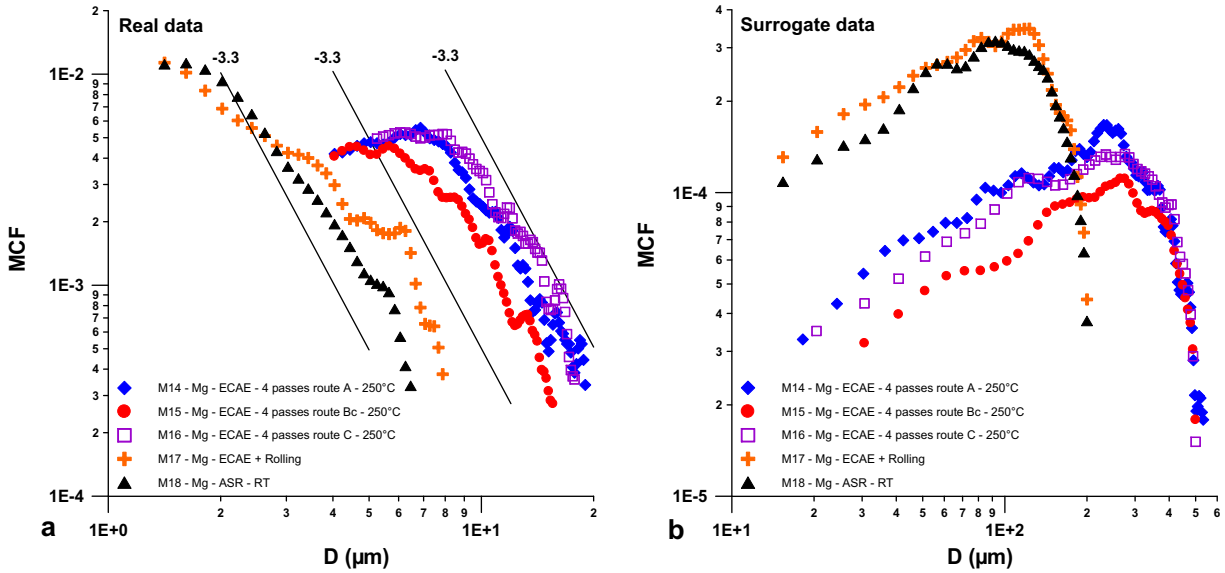


Fig. 7. Misorientation correlation functions (MCF) as function of the distance $D$ for samples where significant DRX took place (samples in Part 3 of Table 1) at preferred misorientation (a) as measured data and (b) surrogate data.

representations of real materials, which are three-dimensional. Apart from strongly anisotropic morphologies, such as lamellar or columnar crystals, two-dimensional maps can, however, be chosen to be representative of the real material morphology. There is also some degree of arbitrariness in the choices made in implementing the analysis. For example, the distance between grains is defined as the distance between their centers of gravity and, as already mentioned, the crystal orientations are defined as averages over their cross-section with the plane of the map to account for intragranular orientation gradients in defining their misorientation. Although other options are possible, these choices do not seem unreasonable if crystal orientation gradients are such that individual grains can be defined at all. It might be argued that we only account for the interactions of a particular grain with its nearest neighbors. If spatial correlations are to be uncovered, one may wonder why they should not extend to more remote grains. However, the origin of the spatial interaction lies in the material contiguity corresponding to intergrain connection. Hence, the probability (Eq. (2)) makes more physical sense when limited to the grain nearest neighbors. Since the correlations quickly decrease with distance, with exponent at least of the order of 2, extending the summation to all pairs of grains would screen short-distance correlations by overwhelming the statistics with large numbers of uncoupled grains.

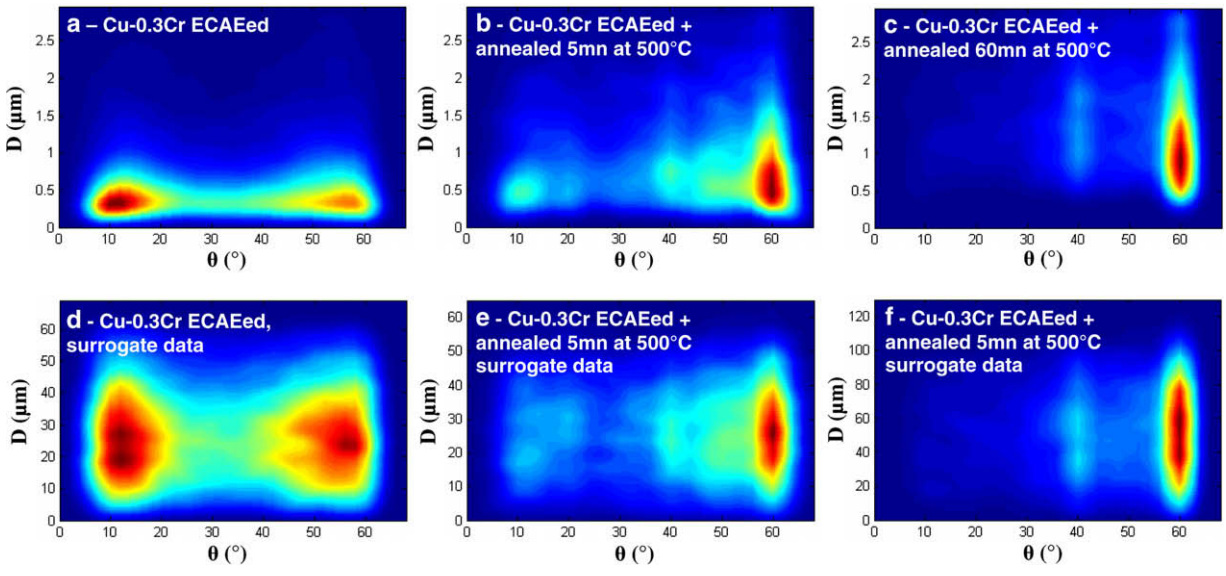


Fig. 8. Iso-levels of the misorientation correlation function (MCF) as function of distance $D$ and misorientation $\theta$ for Cu–0.3Cr samples (samples in Part 4 of Table 1): (a–c) as measured data and (d–f) surrogate data.

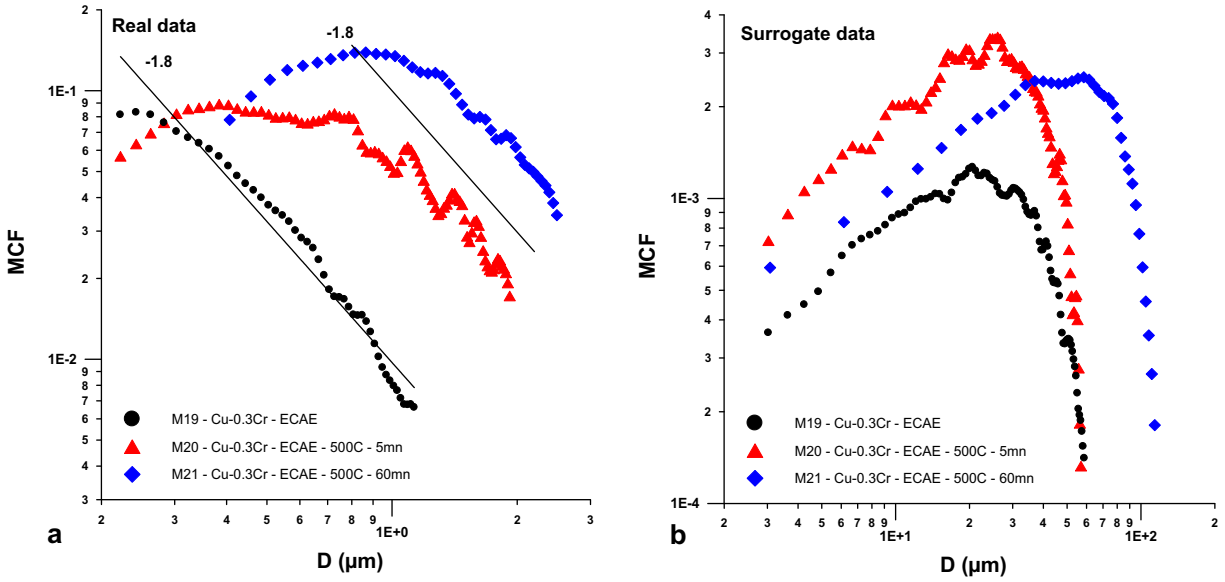


Fig. 9. Misorientation correlation functions (MCF) as function of distance $D$ at $\theta = 60°$ for Cu–0.3Cr samples (samples in Part 4 of Table 1): (a) as measured data and (b) surrogate data.

### 4.2. Slip transmission, strain incompatibility and polar dislocations

A striking feature of the results for strained materials (Part 1 of Table 1) is their apparent "universality". Indeed, scale-invariance of spatial correlations is obtained irrespective of crystal lattice symmetry, deformation process, temperature and strain-rate conditions. These results appear to be valid for fine-grained as well as coarse-grained materials. Hence, the physical origin for the scale-invariant spatial correlations needs to be generic in nature, i.e. not specific to any particular material or loading condition. We conjecture that the constraints on slip transmission at boundaries and the long-range internal stresses due to lattice incompatibility between distinctly oriented neighbor grains are responsible for such a mechanism. Further, the overall intensity of these mechanisms is reflected in the scaling exponent value: the smaller the absolute value of the scaling exponent, the stronger the coupling mechanisms. Lattice curvature and "geometrically necessary dislocations" (hereafter referred to as "polar" dislocations) are associated with such incompatibility. In contrast to polar dislocations, statistical dislocations can be uniformly distributed, and their stress fields statistically offset to a net overall zero contribution to internal stresses. The presence of polar dislocations at boundaries has been proposed in the past [17–19]. We recall that their description is based upon Nye's dislocation density tensor $\boldsymbol{\alpha}$ [20]. The latter is defined from the true Burgers vector $\boldsymbol{b}$ of all dislocations lines threading a surface $S$ of the deformed material configuration, surrounded by a contour $C$ known as the Burgers circuit

$$\mathbf{b} = -\oint_{\mathbf{C}} \mathbf{F}_{\mathbf{e}}^{-1} \cdot \mathbf{dx}. \tag{5}$$

In this relation, $\mathbf{F}_{\mathbf{e}}^{-1}$ is the inverse elastic transformation tensor mapping vectors of the deformed configuration onto vectors of a locally defined elastic-free intermediate configuration [21]. Application of Stoke's relation to Eq. (5) provides

$$\oint_C \mathbf{F}_{\mathbf{e}}^{-1} \cdot \mathbf{dx} = \int\int_S \mathbf{curl}\ \mathbf{F}_{\mathbf{e}}^{-1} \cdot \mathbf{n} dS \tag{6}$$

which allows defining $\boldsymbol{\alpha}$ as a point wise measure for incompatibility through

$$\mathbf{b} = \int\int_S \boldsymbol{\alpha} \cdot \mathbf{n} dS, \quad \boldsymbol{\alpha} = -\mathbf{curl}\ \mathbf{F}_{\mathbf{e}}^{-1}. \tag{7}$$

Because of this incompatibility, the inverse elastic transformation tensor $\mathbf{F}_{\mathbf{e}}^{-1}$ is not a gradient. The property holds also at small strains for the elastic distortion tensor $\mathbf{U}_{\mathbf{e}} \cong \mathbf{I} - \mathbf{F}_{\mathbf{e}}^{-1}$, which we shall also consider in the following for the sake of simplicity. It has an incompatible part, $\mathbf{U}_e^{\perp}$, which is solution to the incompatibility equation derived from Eq. (7) at small strains

$$\mathbf{curl}\ \mathbf{U}_{\mathbf{e}}^{\perp} = \boldsymbol{\alpha} \tag{8}$$

and a compatible part, $\mathbf{U}_e^{\parallel}$, a gradient tensor such that $\mathbf{curl}\ \mathbf{U}_{\mathbf{e}}^{\parallel} = \mathbf{0}$ [22].

In the present context, it is of interest to apply the fundamental relations (5) and (6) to situations where the Burgers circuit $C$ bridges two distinct parts ($H^-$, $H^+$) of a crystalline material across a surface of discontinuity $I$, typically a grain boundary. As is well known, conventional continuum mechanics requires continuity of stress and displacement at the interface $I$, but incompatible distortion associated with the presence of polar dislocations is usually overseen. Following a scheme initiated in Refs. [17,18] and revisited in Ref. [23] in a dynamical perspective, let us con-

sider the Burgers circuit sketched in Fig. 10. The unit vector $n$ normal to the interface $I$ is oriented from $H^-$ to $H^+$ and $l$ is an arbitrary unit vector lying in the interface. The Burgers circuit is a rectangle of length $L$ in the direction of vector $l$ and width $h = h^- + h^+$ in the transverse direction, oriented by the cross product $\mathbf{n} \times \mathbf{l}$ ($H^-$ and $H^+$ have respective width $h^-$ and $h^+$). According to relations (5) and (6), it is seen that

$$\forall \mathbf{l} \in I, \int \int_S \boldsymbol{\alpha} \cdot (\mathbf{n} \times \mathbf{1}) dS = -\oint_C \mathbf{F}_e^{-1} \cdot \mathbf{dx}. \tag{9}$$

Let us assume that a continuous distribution of polar dislocations exists on both sides of the interface, as well as a singular distribution of surface dislocations $\boldsymbol{\alpha}(I)$ along the interface. The limit of continuous fields approaching the interface $I$ from above is assigned the superscript "$^+$", and that of fields approaching $I$ from below the superscript "$^-$". Hence, the discontinuity in a field $\boldsymbol{x}$ at the interface is denoted $[\boldsymbol{x}] = \boldsymbol{x}^+ - \boldsymbol{x}^-$. Note that the components of the distribution $\boldsymbol{\alpha}(I)$ of surface dislocations are expressed as the non-dimensional ratio of a Burgers vector length $nb$ over a segment length $L$ in the direction of unit vector $\mathbf{l}$, whereas the components $\alpha_{ij}$ of tensor $\boldsymbol{\alpha}$ have dimension $\mathrm{m}^{-1}$ (Burgers vector length over unit area $\mathrm{m}^{-2}$). In the limit of the Burgers circuit collapsing onto point P when $h^-$, $h^+$ tend to zero and $L$ shrinks along $\mathbf{l}$, relation (9) becomes

$$\forall \mathbf{l} \in I,\ \boldsymbol{\alpha}(I) \cdot \mathbf{n} \times \mathbf{l} = -[\mathbf{F}_e^{-1}] \cdot \mathbf{l}. \tag{10}$$

Using the tensor cross product $\mathbf{A} \times \mathbf{n}$ defined as: $\forall \mathbf{l},\ (\mathbf{A} \times \mathbf{n})^t \cdot \mathbf{l} = \mathbf{A}^t \cdot \mathbf{l} \times \mathbf{n}$, relation (10) can also be written in the form:

$$\forall \mathbf{l} \in I,\ (\boldsymbol{\alpha}^t(I) \times \mathbf{n})^t \cdot \mathbf{l} = [\mathbf{F}_e^{-1}] \cdot \mathbf{l} \tag{11}$$

or, equivalently,

$$(\boldsymbol{\alpha}^t(I) \times \mathbf{n})^t \times \mathbf{n} = [\mathbf{F}_e^{-1}] \times \mathbf{n}. \tag{12}$$

This relation between the dislocation content of the interface and the jump in the inverse elastic transformation it accommodates can be thought of as a generalized Frank–Bilby relation [17,18]. To see this, assume for example that the elastic deformation be negligible on both sides of the interface. Hence, the material deforms in a purely viscoplastic manner and the elastic transformation tensor reduces to its orthogonal part: $\mathbf{F}_e = \mathbf{R}_e$, $\mathbf{R}_e^{-1} = \mathbf{R}_e^t$, which represents material rotation. For the sake of simplicity, we shall further assume infinitesimal rotations. Then $\mathbf{F}_e^{-1} = \mathbf{R}_e^t \cong \mathbf{I} - \boldsymbol{\omega}_e$, where $\boldsymbol{\omega}_e$ is the skew-symmetric part of the elastic distortion tensor $\mathbf{U}_e$, i.e., the elastic spin tensor. Introducing the equivalent elastic spin vector $\boldsymbol{\Omega}_e$ such that: $\forall \mathbf{l},\ \boldsymbol{\omega}_e \cdot \mathbf{l} = \boldsymbol{\Omega}_e \times \mathbf{l}$, relation (11) becomes.

$$\forall \mathbf{l} \in I,\ (\boldsymbol{\alpha}^t(I) \times \mathbf{n})^t \cdot \mathbf{l} = -[\boldsymbol{\Omega}_e] \times \mathbf{l}. \tag{13}$$

Eq. (13) provides the dislocation content of the interface accommodating the discontinuity in the elastic spin, which essentially achieves the purpose of Frank's relation. For example, assume that the jump in elastic spin belongs to the interface, say: $[\boldsymbol{\Omega}_e] = \theta\ \mathbf{n} \times \mathbf{l}$. Then $[\boldsymbol{\Omega}_e] \times \mathbf{l} = \theta\ (\mathbf{n} \times \mathbf{l}) \times \mathbf{l} = -\theta\ \mathbf{n}$, and the left-hand side of Eq. (13) is $(\boldsymbol{\alpha}^t(I) \times \mathbf{n})^t \cdot \mathbf{l} = \theta\ \mathbf{n}$, or equivalently: $\boldsymbol{\alpha}(I) \cdot \mathbf{l} \times \mathbf{n} = \theta\ \mathbf{n}$. Defining the singular dislocation density $\boldsymbol{\alpha}(I)$ as: $\boldsymbol{\alpha}(I) = (nb/L)\mathbf{b} \otimes \mathbf{t}$, where $\mathbf{B} = (nb/L)\mathbf{b}$ is the Burgers vector and $\mathbf{t}$ the line vector (b and t being unit vectors), it is seen from the last equation that $\mathbf{b} = \mathbf{n}$, $\mathbf{t} = \mathbf{l} \times \mathbf{n}$ and $L/n = b/\theta$. Hence, the surface dislocation density $\boldsymbol{\alpha}(I)$ describes the interface $I$ as a tilt boundary, composed of edge dislocations with line direction aligned with the elastic spin and Burgers vector normal to the interface. The well-known relation $L/n = b/\theta$ describes the spacing of dislocations in the tilt boundary. In such a model, the interface is viewed as having no width, and any jump in rotation between the neighboring crystals can be accommodated by a singular dislocation distribution, by just choosing the appropriate dislocation spacing according to Frank's relation. Hence, this model does not predict any correlation in the rotation of neighboring crystals. In contrast, if the intent is to describe the grain boundary as a region of finite width, the notion of a singular dislocation density must be surrendered, and the distribution of the dislocation density in the interface area must be considered as continuous in both crystals $H^-$ and $H^+$ (as well as other field variables). In the context of such a continuous model for grain boundaries, the generalized Frank–Bilby relation (12) becomes

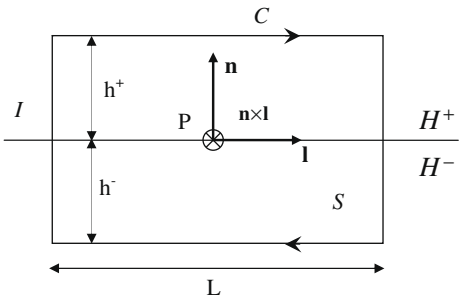


Fig. 10. Sketch of interface $I$ between sub-domains ($H^-$, $H^+$), with normal vector $\boldsymbol{n}$. The unit vector $\boldsymbol{l}$ is an arbitrary vector in the interface. The Burgers circuit $C$ surrounds surface $S$ bridging over the interface $I$, and oriented by the cross-product $\mathbf{n} \times \mathbf{l}$ normal to surface $S$.

$$[\mathbf{F}_e^{-1}] \times \mathbf{n} = \mathbf{0} \tag{14}$$

or equivalently

$$\forall \mathbf{l} \in I,\ [\mathbf{F}_e^{-1}] \cdot \mathbf{l} = \mathbf{0}. \tag{15}$$

Whereas in the singular representation of a grain boundary, there is no material continuity along the interface, Eq. (15) implies "tangential continuity" across the interface. Indeed, the inverse elastic mapping of any tangential material vector of the deformed configuration must lead to the same material vector on both sides of the interface. Using the standard elastic–plastic decomposition of the transformation gradient tensor $\mathbf{F} = \mathbf{F}_e \cdot \mathbf{F}_p$ [24], the tangential continuity condition ((14) and (15)) on $\mathbf{F}_e^{-1}$ can be complemented by a reverse condition on $\mathbf{F}_p$. Indeed, continuity of the displacement is required by continuum mechanics,

which implies that the inverse transformation gradient $\mathbf{F}^{-1}$ satisfies tangential continuity along the interface

$$[\mathbf{F}^{-1}] \times \mathbf{n} = \mathbf{0} \text{ or } \forall \mathbf{l} \in I, \quad [\mathbf{F}^{-1}] \cdot \mathbf{l} = \mathbf{0} \tag{16}$$

a condition commonly referred to as Hadamard's kinematic compatibility condition [25]. Hence, the jump $[\mathbf{F}_e^{-1}]$ in the elastic transformation tensor is offset by a jump $[\mathbf{F}_p]$ in the plastic transformation tensor satisfying the relation

$$\forall \mathbf{l} \in I, \ [\mathbf{F}_e^{-1}] \cdot \mathbf{l} = [\mathbf{F}_p] \cdot \mathbf{F}^{-1} \cdot \mathbf{l} + \mathbf{F}_p \cdot [\mathbf{F}^{-1}] \cdot \mathbf{l} = \mathbf{0} \tag{17}$$

or, substituting Eq. (16) in Eq. (17),

$$\forall \mathbf{l_0} \in I_0, \ [\mathbf{F}_p] \cdot \mathbf{l_0} = \mathbf{0}, \ \mathbf{l_0} = \mathbf{F}^{-1} \cdot \mathbf{l}. \tag{18}$$

Here ($\mathbf{l_0}$, $I_0$) are the images of ($\mathbf{l}$, $I$) in the reference configuration, mapped from ($\mathbf{l}$, $I$) through the inverse transformation gradient. If $\mathbf{n_0}$ is a vector normal to the interface $I_0$ in the reference configuration, Eq. (18) is equivalent to

$$[\mathbf{F}_p] \times \mathbf{n_0} = \mathbf{0}. \tag{19}$$

In order to understand the implications of the result (Eqs. (14)–(19)), it may be useful to reconsider the example of a purely viscoplastic material submitted to infinitesimal transformations. Eq. (13), which is relevant to that case, now becomes

$$\forall \mathbf{l} \in I, \quad [\mathbf{\Omega}_e] \times \mathbf{l} = \mathbf{0} \tag{20}$$

which implies

$$[\mathbf{\Omega}_e] = \mathbf{0}. \tag{21}$$

Hence, continuity of the elastic spin is required across the interface. This condition can also be retrieved from the dynamic continuity condition set out in Ref. [23] (see Refs. [26,27]). Thus, although a singular model is eligible, a more accurate (continuous) description of the grain boundary implies the existence of spatial correlations between neighboring crystals, because limiting values of the elastic spin from the two sides of the surface of discontinuity are required to be equal. When material elasticity is included in the description, the correlation in crystal rotation is less stringent than the strict co-rotation implied by Eq. (21). Indeed, still assuming infinitesimal transformations, Eq. (15) becomes in that case

$$\mathbf{U}_e \times \mathbf{n} = \mathbf{0}, \ \forall \mathbf{l} \in I, \ [\mathbf{\Omega}_e] \times \mathbf{l} = -[\boldsymbol{\varepsilon}_e] \cdot \mathbf{l}. \tag{22}$$

Projecting onto the orthogonal frame ($\boldsymbol{e_1} = \boldsymbol{l}$, $\boldsymbol{e_2} = \boldsymbol{n} \times \boldsymbol{l}$, $\boldsymbol{e_3} = \boldsymbol{n}$), one obtains in component form

$$[\Omega_1^e] = [\varepsilon_{23}^e], \ [\Omega_2^e] = [\varepsilon_{31}^e], \ [\Omega_3^e] = [\varepsilon_{12}^e]. \tag{23}$$

Here, $\boldsymbol{\varepsilon}_e$ is the symmetric part of the elastic distortion tensor $\mathbf{U}_e$, i.e., the elastic deformation tensor. Like $\mathbf{U}_e$, $\boldsymbol{\varepsilon}_e$ has an incompatible part, $\boldsymbol{\varepsilon}_e^{\perp}$, due to the presence of polar dislocations, and a compatible part, $\boldsymbol{\varepsilon}_e^{\parallel}$, which contributes to the solution of the elasto-plastic boundary value problem. Due to the presence of $\boldsymbol{\varepsilon}_e^{\perp}$, Eqs. (22) and (23) show that the jump in elastic spin across the grain boundary is dependent on the presence of polar dislocations in this area. Such a result comes in full support of the conjecture presented up front in this section. It shows that a consistent theory of texture development needs to have non-local character, and that the latter derives from lattice incompatibility in the grain–boundary region.

Gradients in the elastic spin are in direct relation with the polar dislocation content, as testified by the following relation [21]:

$$\mathbf{grad}\ \mathbf{\Omega}_e = \mathbf{curl}\ \boldsymbol{\varepsilon}_e^t - \left(\boldsymbol{\alpha}^t - \frac{1}{2} tr(\boldsymbol{\alpha})\mathbf{I}\right). \tag{24}$$

Hence, the above conjecture can be experimentally verified by investigating intragranular lattice rotation gradients, particularly in the vicinity of grain boundaries. The procedure is the very same as that utilized in Section 3 for grain-to-grain misorientation. An example is presented in Fig. 1 for a large grain in Material 4 (compressed titanium). Two oriented lines were selected (see Fig. 3) along which misorientation with respect to the dot-marked reference point was calculated. Along Line 1, the misorientation remains nearly constant (less than 2–3° variation) on the first 50 μm then strongly increases to finally reach 28° close to the opposite grain boundary. On Line 2, larger fluctuations (4–5°) are seen in the first 120 μm then, similar to Line 1, the misorientation increases by about 20° in 20 μm close to the grain boundary. These strong gradients are indication of the presence of a large density of polar dislocations in the neighborhood of grain boundaries, which is supporting the views expressed earlier. Note that the length scale over which the influence of the tangential continuity conditions (14), (22) and (23) reaches into the material is not implied by these conditions. The scaling laws uncovered in Section 3 as well as the above measurements show that it extends well into the first neighbor grains. Similar measurements described in Ref. [28] also support these views.

### 4.3. Incidental dislocation boundaries

On average, the incidental dislocation boundaries (IDBs), which separate dislocation cells and develop small misorientation angles, were not considered in the present paper, because, as already mentioned, the minimum misorientation angle was set to a much larger value: 5°. However, the relative absence of correlation noticed above for small misorientation angles is consistent with their properties. Indeed, IDBs are thought to form by statistical trapping of glide dislocations, a mechanism not involving the lattice incompatibility associated with the presence of polar dislocations [29–31]. Further, plots of scaled IDB distributions reveal the existence of a universally preferred misorientation [29–31], a property at odds with the scale-invariance shown here for high-angle boundaries. Note that the higher-angle boundaries between dislocation cells referred to as "geometrically necessary boundaries" do not convincingly show the same statistical features as IDBs [29–31], which is again consistent with the present under-

standing. Finally, there is no obstacle to extending the present analysis to dislocation cell boundaries by setting the minimum misorientation angle to a value smaller than 5°.

### 4.4. Effect of grain refinement during large plastic strain

Severe plastic deformation (SPD) not only leads to the formation of dislocation cells and IDBs but usually results in the fragmentation of the grains that initially compose the polycrystal. At extreme strains, an outcome of grain refinement can be the production of ultra-fine-grained polycrystals with exceptional mechanical properties (see a review of SPD processes in Ref. [32]). ECAE is one of the most promising techniques that are used for this purpose. Large part of our database was obtained by using this technique and substantial amount of grain size reduction is believed to have taken place in those tests.

Grain refinement can be looked at as a result of lattice incompatibility developing in the initial grains. The gradual increase in misorientation across initial sub-grain boundaries can be attributed to pile-ups of the polar dislocations that produce lattice curvature in this area. It is plastic strain which drives the progressive transformation of low-angle sub-grain boundaries into high-angle boundaries. As shown above, this process changes dramatically the MCF, whose character shifts from uncorrelated to spatially correlated. While it cannot be excluded that the new grains keep the misorientation of their parent grains during fragmentation, polar dislocations are still present in their new boundary area, with the consequences described in Section 4.2. The continuity constraints lead to an orientational relationship between the new grains. This interaction is expected to be stronger near to the grain boundary, which suggests that the orientational constraint should be more stringent in smaller grains.

### 4.5. Effect of annealing: low-angle boundaries

Since one of the most prominent effects of annealing is to relax internal stresses, the above conjecture is also confirmed a contrario by the absence of spatial correlations apparent in Fig. 6 in samples annealed after straining. Further support to the conjecture is obtained from Fig. 9, which provides evidence for the decay of spatial correlations and the shortening of the scaling range when the annealing treatment is made stronger. Additional arguments in support of the conjecture can be made from the faster decay (or absence) of spatial correlations in the case of low-angle grain boundaries and in samples undergoing dynamic recrystallization (DRX) (Fig. 7). Indeed, low-angle grain boundaries are considered as being associated with low intensity of internal stresses, and one of the primary effects of DRX is to lower this intensity level in the recrystallized grains by erasing incompatible lattice rotation gradients.

### 4.6. Grain-size dependence

The presence of polar dislocations at grain boundaries as a result of constraints on grain-to-grain slip transmission has been recognized as being of primary significance in the interpretation of the grain-size dependence of the flow stress, i.e. the Hall–Petch effect. Indeed, boundaries act as strong barriers to dislocation motion, as evidenced by dislocation pile-ups. The propagation of plastic slip activity across grain boundaries by activation of sources in neighbor grains is also thought to be related to the internal stresses originating from these dislocation pile-ups, a phenomenon commonly used to explain the propagation of Lüders bands. Interactions between polar dislocations and grain boundaries are even more complex when boundaries are set into motion through twinning or dynamic recrystallization. It is to be mentioned here that power law statistics have also been shown to characterize the scale-invariant self-organization of plastic activity in ice polycrystals, as reflected by the associated acoustic emission [33]. In this paper, the property was ascribed to spatial correlations in relation with long-range interactions and incompatible lattice distortion. Although the average grain size sets an internal length scale reflecting a barrier to dislocation motion, the authors have shown that the self-organized character of plastic activity extends towards length scales much larger than the average grain size [33], which comes in support of the present findings.

### 4.7. Effect on texture strength

By appending the elastic spin continuity condition (20) to the framework of a finite deformation crystal viscoplastic finite element setting, Mach et al. [26] have predicted texture development in rolling simulations for face-centered cubic (fcc) metals. Their results reproduce the trend already alluded to in the present paper to reduced intensity of the predicted crystallographic texture with respect to Taylor-type or viscoplastic self-consistent type predictions, and match more closely the experimental data. Including incompatible lattice distortion in the continuity conditions, as done in Eqs. (21) and (22), might lead to an additional improvement of the predictions. Another direct consequence of the grain-to-grain spatial correlation evidenced in this paper is that the strength of the crystallographic texture should be higher in coarse-grained than in fine-grained materials. Indeed, the large value of the probability for encountering a specific boundary pattern at short intergranular distances limits the propensity of the straining path to generate marked textures in fine-grained materials. Experimental evidence of a grain size effect on texture strength can be found in recent papers [34,35]. Jain et al. [34] show that the texture strength index increases with grain size in magnesium alloy AZ31B after annealing (Table 1, Ref. [34]) and suggest that this issue is critical in the grain-size dependence of the twin volume fraction after tensile loading. Park and Szpunar [35] provide similar

information for the cold rolling textures developed in two samples of electrical steel: Fig. 2 of Ref. [35] shows a much stronger texture component in the large grained steel than in the fine-grained steel. These authors also suggest that this difference can be considered as being inherited from the texture difference between the two steels in the annealed state. Similar observation was reported by Anderson et al. [36] while examining rolling texture of Cu/Nb polycrystalline multilayers with variable thicknesses, where the Kurdjumov–Sachs orientation relationship was valid across the fcc/bcc interface. The experimental rolling textures indicated that the Kurdjumov–Sachs relation was lost for the "thick" layers, while it was preserved to a large degree for the "thin" layers, which is consistent with the trends implied by our scaling relations.

## 5. Conclusion

Scaling laws have been uncovered in the distribution of grain misorientation vs. inter-granular distance in various materials under diverse loading paths corresponding to different processing methods. In the absence of annealing, the scaling exponent is of the order of $\tau = 2 \pm 0.3$ for high-angle grain boundaries, however, it increases (in absolute value) for low-angle grain boundaries, or under dynamic recrystallization. Sequential annealing after deformation leads to uncorrelated distributions. These results argue for inter-granular scale-free spatial correlations through constraints on slip transmission across boundaries, long-range internal stresses due to strain incompatibility between distinctly oriented neighbor grains, and for lattice curvature associated with the presence of polar dislocations at grain boundaries. In the framework of a field dislocation theory, such correlation assumes the form of tangential continuity conditions on the inverse elastic transformation tensor or on the plastic transformation tensor, in the deformed and reference configurations respectively. In an infinitesimal transformation setting, these conditions provide the jump in the elastic spin vector across the boundary as a function of the jump in the incompatible elastic distortion.

Implications of the scale-invariant law on misorientation vs. inter-granular distance and grain-to-grain continuity conditions are the trend to milder texture development, and the size dependence of the latter. The coarser the grain structure, the stronger is the texture induced by the strain path. Several experimental verifications of the effect were provided; however, a more systematic investigation is still desirable. From the point of view of modeling, our results imply that a consistent theory of texture development needs to have non-local character, since limiting values of elastic spin on both sides of a grain boundary should have a relationship.

## Acknowledgments

The authors would like to acknowledge the Department of Science and Technology (DST), Government of India for providing financial grant for a part of this project. The work also used the facility set up under Institute Nanoscience Initiative sponsored by DST-FIST program at IISc, Bangalore. The authors gratefully acknowledge Satyaveer Singh Dhinwal and Somjeet Biswas (IISc, Bangalore) for their help in the experiments, Armand J. Beaudoin, Louisette Priester, Thiebaud Richeton and Anthony D. Rollett for their suggestions and careful reading of the manuscript.

## Appendix. Supplementary material

A Fortran program for the calculation of the Misorientation Correlation Function can be found at www.benoit-beausir.e3b.org.

## References

[1] Mackenzie JK. Biometrika 1958;45:229.
[2] Gertsman VY, Tangri K. Acta Metall Mater 1995;43:2317.
[3] Ryoo HS, Hwang SK, Kim MH, Kwun SI, Chae SW. Scr Mater 2001;44:2583.
[4] Alley RB, Gow AJ, Meese DA. J Glaciol 1995;41:197.
[5] Durand G, Persson A, Samyn D, Svenssson A. Earth Planet Sci Lett 2008;265:666.
[6] Winther G, Margulies L, Schmidt S, Poulsen HF. Acta Mater 2004;52:2863.
[7] Hill R. J Mech Phys Solids 1965;13:89.
[8] Bolmaro RE, Lebensohn RA, Brokmeier HG. Comp Mater Sci 1997;9:237.
[9] Tomé CN, Lebensohn RA, Necker CT. Metall Mater Trans 2002;33A:2635.
[10] Bolmaro RE, Fourty A, Signorelli JW, Brokmeier HG. Mater Sci Eng 2006;14:1.
[11] Signorelli JW, Turner PA, Sordi V, Ferrante M, Vieira EA, Bolmaro RE. Scr Mater 2006;55:1099.
[12] Delannay L, van Houtte P, Samajdar I. J Phys IV 1999;9:43.
[13] van Houtte P, Delannay L, Samajdar I. Textures Microstruct 1999;31:109.
[14] van Houtte P, Li S, Seefeldt M, Delannay L. J Int Plast 2005;21:589.
[15] Adams BL, Morris PR, Wang TT, Willden KS, Wright SI. Acta Metall 1987;35:2935.
[16] Bunge HJ. Texture analysis in materials science. London: Butterworth; 1982.
[17] Frank FC. In: Symposium on the plastic deformation of crystalline solids. Pittsburgh: Mellon Institute; 1950. p. 150 [NAVEXOS-P-834].
[18] Bilby BA. Bristol conference report on defects in crystalline solids. London: The Physical Society; 1955. p. 123.
[19] Ashby MF. Philos Mag 1970;21:399.
[20] Nye JF. Acta Metall 1953;1:153.
[21] Kröner E. Continuum theory of defects in physics of defects. In: Balian R et al., editors. Les Houches, Session XXXV, 1980. North Holland Publishing Company; 1981.
[22] Acharya A. J Mech Phys Solids 2001;49:761.
[23] Acharya A. Philos Mag 2007;87:1349.
[24] Lee EH. J Appl Phys 1969;36:1.
[25] Hadamard J. Leçons sur la propagation des ondes et les équations de l'hydrodynamique. Paris: Herman; 1903.
[26] Mach J, Beaudoin AJ, Acharya A. Continuity in the plastic strain rate and its influence on texture evolution. J Mech Phys Solids; in press.
[27] Mach J. PhD thesis, University of Illinois at Urbana Champaign, 2009.
[28] Mishra SA, Pant P, Narasimhan K, Rollett AD, Samajdar I. Scr Mater 2009;61:273–6.

[29] Hughes DA, Liu Q, Chrzan DC, Hansen N. Acta Mater 1997;45:105–12.
[30] Hughes DA, Liu Q, Chrzan DC, Hansen N. Phys Rev Lett 1998;81:4664–7.
[31] Godfrey A, Hughes DA. Scr Mater 2004;51:831–6.
[32] Valiev RZ, Langdon TG. Prog Mater Sci 2006;51:881–981.
[33] Richeton T, Weiss J, Louchet F. Nature Mater 2005;4:465.
[34] Jain A, Duygulu O, Brown DW, Tomé CN, Agnew SR. Mater Sci Eng 2008;486A:545.
[35] Park JT, Szpunar JA. J Magn Magn Mater 2008;321:1928.
[36] Anderson PM, Bingert JF, Misra A, Hirth JP. Acta Mater 2003;51:6059.